Covalent organic frameworks for design of ruthenium catalysts with high single-atom site density for CO 2 hydrogenation into formic acid

Ana Fellenberg, Ahmed Addad, Sergei A. Chernyak, Zhou Yong, Massimo Corda, Danilo Oliveira de Souza, Olga V. Safonova, Vlad Martin-Diaconescu, Vitaly Ordomsky, Gang Ji, et al.

Cell Reports
Physical Science

CellPress
OPEN ACCESS

Article

Covalent organic frameworks for design of ruthenium catalysts with high single-atom site density for CO_2 hydrogenation into formic acid

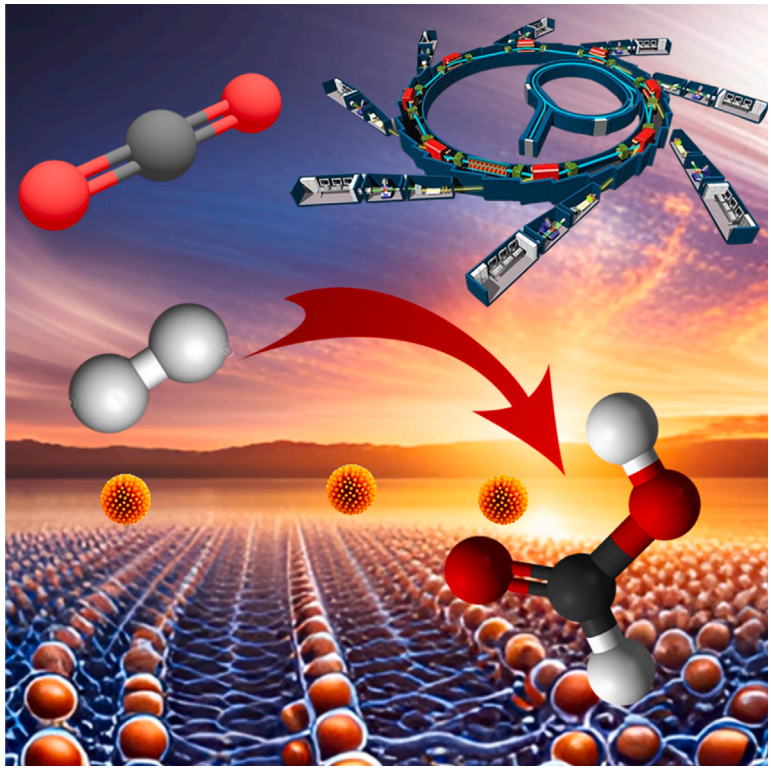

Carbon dioxide is an abundant resource for chemical and fuel synthesis, for example the synthesis of formic acid. Here, Fellenberg et al. present a strategy that utilizes covalent organic frameworks with diverse structures and chemical compositions to enhance carbon dioxide hydrogenation to formic acid at low temperatures.

Ana Katiuce Fellenberg, Ahmed Addad, Sergei A. Chernyak, ..., Vitaly V. Ordomsky, Gang Ji, Andrei Y. Khodakov

gang.ji@univ-lille.fr (G.J.)
andrei.khodakov@univ-lille.fr (A.Y.K.)

Highlights

Strategy to improve activity of ruthenium catalysts for CO_2 hydrogenation

High density and intrinsic activity of ruthenium single-site sites in COFs

Intrinsic activity of single-atom sites is affected by nitrogen functional groups

Catalyst stability is attributed to the ability of single atoms to resist reduction

Fellenberg et al., Cell Reports Physical Science 5, 101926
April 17, 2024
https://doi.org/10.1016/j.xcrp.2024.101926

Cell Reports
Physical Science

CellPress
OPEN ACCESS

Article

Covalent organic frameworks for design of ruthenium catalysts with high single-atom site density for CO_2 hydrogenation into formic acid

Ana Katiuce Fellenberg,[1] Ahmed Addad,[2] Sergei A. Chernyak,[1] Yong Zhou,[1] Massimo Corda,[1] Danilo Oliveira De Souza,[1,3] Olga V. Safonova,[4] Vlad Martin-Diaconescu,[5] Vitaly V. Ordomsky,[1] Gang Ji,[2,*] and Andrei Y. Khodakov[1,6,*]

SUMMARY

Carbon dioxide is an abundant carbon resource for chemical and fuel synthesis. Formic acid, vital for hydrogen storage, has numerous applications. Covalent organic frameworks are a unique class of materials composed of interconnected organic building blocks through covalent bonds. They possess porosity and functional groups, making them suitable for creating supported metallic catalysts. In this study, we present a strategy that utilizes covalent organic frameworks with diverse structures and chemical compositions to enhance carbon dioxide hydrogenation to formic acid at low temperatures. This enhancement arises from both high density of single-atom ruthenium sites and their intrinsic activity. Operando X-ray absorption and catalytic tests demonstrate that the concentration of nitrogen functional groups affects the intrinsic single-site ruthenium activity, whereas the impact of oxygen-containing groups is minor. Catalyst stability is attributed to the ability of single atoms to resist reduction to metallic state. This strategy has broad applicability for various covalent organic framework-supported single-atom catalysts.

INTRODUCTION

Covalent organic frameworks (COFs)[1–3] are dense, porous polymers with definite 2D and 3D crystalline structures composed of light elements (B, N, C, and O) linked via covalent bonds that exhibit many interesting characteristics, such as high surface area, porosity in a small mesopore range, presence of several functional groups, and versatile chemistry. They have triggered significant research perspectives toward energy applications attributed to their unique physiochemical properties. The tunable structure, inherent pores, and superior strong covalent bonds of COFs give them an advantage over other crystalline porous materials such as metal-organic frameworks (MOFs), mesoporous silica, and zeolites. Compared to MOFs, COFs have excellent stability both in organic solvents and in extreme alkaline and acid solutions. COFs seem to be analogous to the enzyme-type systems.

Recent years have witnessed a spectacular growth of single-atom catalysts (SACs)[4–9] as a conceptual bridge filling the gap[10,11] between homogeneous and heterogeneous catalysis. Various terms have been employed[12] to characterize these catalysts, such as single-site heterogeneous catalysts,[13] atomically dispersed supported metal catalysts,[14] or site-isolated heterogeneous catalysts.[15] In this study, we will adopt the

[1]University of Lille, CNRS, Centrale Lille, University of Artois, UMR 8181 (UCCS) Unité de Catalyse et Chimie du Solide, Lille, France

[2]University of Lille, CNRS, INRAE, Centrale Lille, UMR 8207 (UMET) Unité Matériaux et Transformations, 59000 Lille, France

[3]Elettra-Sincrotrone Trieste, Strada Statale 14, km 163.5, 34149 Basovizza, Trieste, Italy

[4]PSI, 5232 Villigen, Switzerland

[5]ALBA Synchrotron Light Source, Crta. BP 1413, Km. 3.3, 08290 Cerdanyola Del Vallès, Barcelona, Spain

[6]Lead contact

*Correspondence: gang.ji@univ-lille.fr (G.J.), andrei.khodakov@univ-lille.fr (A.Y.K.)

https://doi.org/10.1016/j.xcrp.2024.101926

term SAC, denoting the atomically dispersed metal on a support. SACs have several advantages relative to the conventional homogeneous and heterogeneous systems, such as a maximum atom utilization efficiency, absence of any metal-metal bonds, and unique tunable active sites compared to homogeneous organometallic complexes. Their well-defined active sites can be downsized to nanoscale and sub-nanoscale. Anchoring single-metal sites in SACs occurs on vacancies or functional groups on the support surface. Practical applications of Ru SACs suffer from a low metal loading (<2 wt %).[16,17] Due to the elevated surface energy and the consequent propensity for single-metal atoms to easily aggregate, constructing high-density Ru SACs has been challenging. While COF-supported catalysts have found applications[18–24] in electro- and photo-catalysis, there is very limited information[25–27] available on the catalytic performance of SACs supported by COFs in thermocatalytic reactions.

The current growing attention to global climate changes, growing energy demands, and dwindling oil reserves have spurred major research efforts in academia and industry focused on the carbon dioxide capture and utilization technologies. Carbon dioxide (abbreviated as CO_2) is an abundant and vital carbon resource that can be profitable for various chemical, material, and catalytic applications.[28–32] Due to the chemical inertness of CO_2 and high energy barrier, the conversion of CO_2 into high-value-added chemicals is still facing huge challenges. Formic acid produced from CO_2 hydrogenation is an important biodegradable sustainable feedstock. Anhydrous formic acid possesses energy density comparable to that of liquefied hydrogen, making it suitable for both hydrogen storage and generation. Formic acid has found applications in various fields, including the design of direct formic acid fuel cells, as well as in the textile, pharmaceutical, agriculture, leather, and food chemistry industries. The current commercial process, which produces 800,000 tons of formic acid annually,[33–35] involves the use of methanol, toxic carbon monoxide, and corrosive sodium methoxide.

In this study, we propose a strategy to enhance ruthenium dispersion and achieve a higher single-atom density within various COF structures and compositions. This approach aims to design highly active catalysts for CO_2 hydrogenation, specifically targeting the formation of formic acid. (Figure 1). The catalysts were characterized using a combination of techniques including *operando* X-ray absorption spectroscopy. The amount of single-atom sites and concentration of nitrogen functional groups in the COF matrix were found to be key factors to obtain enhanced catalytic performance. The catalyst's stability was linked to ruthenium's capability to remain as single atoms and to resist reduction to the metallic phase.

RESULTS AND DISCUSSION

Ex situ catalyst characterization

The synthesis procedures and detailed characterization of COF materials used in this work as catalytic supports are given in the supplemental experimental procedures: X-ray diffraction (XRD) patterns, high-angle annular dark-field scanning transmission electron microscope (HAADF-STEM) images, cross-polarization magic-angle spinning (CP/MAS), ^{13}C nuclear magnetic resonance (NMR) spectra, attenuated total reflectance Fourier transform infrared (ATR-FTIR) spectra, nitrogen adsorption isotherms, and thermogravimetric analyzer (TGA) curves (Figures S1–S6). The elemental composition of prepared Ru/COF samples measured by X-ray fluorescence (XRF) analysis is shown in Table S1. In addition to ruthenium, the catalysts contain carbon and nitrogen, which were already present in the parent COF materials. The N/Ru molar ratios were calculated from the amounts of nitrogen and

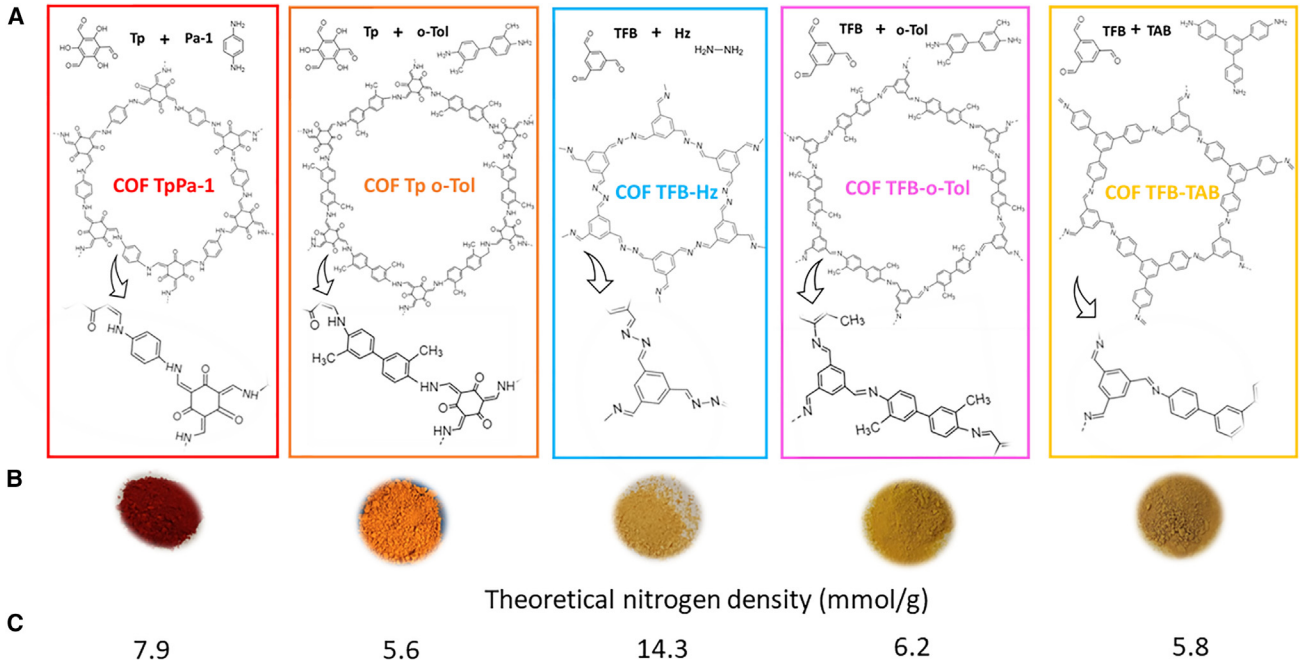

Figure 1. COFs synthesized in this work
(A) Molecular structure.
(B) Visual aspects.
(C) Theoretical nitrogen density (mmol/g).

ruthenium measured by XRF (experimental N/Ru ratio in the fresh samples) and from the theoretic concentration of nitrogen calculated from the COF chemical formula and Ru experimental concentration (theoretic N/Ru ratio). Note that these theoretic and experimental N/Ru ratios are very close to each other and follow the same trend (Table S1). Interestingly, the experimental N/Ru values are somewhat lower than the theoretic ones. This can be attributed to the partial amorphization of the samples during their preparation, also observed by XRD.

The crystalline structure of COF is distinctly affected by introduction of ruthenium. Broadening of the XRD peaks was observed after impregnating COF with $RuCl_3$ (Figure S2). The $RuCl_3$ deposition can possibly block the pores and may result in less-effective π-π stacking interactions between adjacent layers. This may result in a lateral shift of the COF 2D sheets and reduce the crystallinity of COF.[36]

In addition to the crystallinity, the COF morphology undergoes a noticeable change after impregnation with ruthenium and during the CO_2 hydrogenation. The introduction of Ru and conducting CO_2 hydrogenation appear to alter the arrangement of the framework structures, causing misalignment and shifting of the 2D sheets. This suggestion is consistent with nitrogen adsorption measurements. The Brunauer-Emmett-Teller (BET) surface areas of COF have been significantly modified by the impregnation with ruthenium chloride (Table S2). Interestingly, the presence of $RuCl_3$ may result either in an increase or in a decrease in the COF surface area depending on the specific interactions between $RuCl_3$ and the COF material. The observed increase in the 1,3,5-triformylphloroglucinol (Tp) *o*-tolidine (*o*-Tol) and benzene-1,3,5-tricarboxaldehyde (TFB) hydrazine (Hz) COF surface area after the $RuCl_3$ impregnation (Table S2) could be explained by modification of their film-like morphology and creation of interlayer voids after the impregnation.

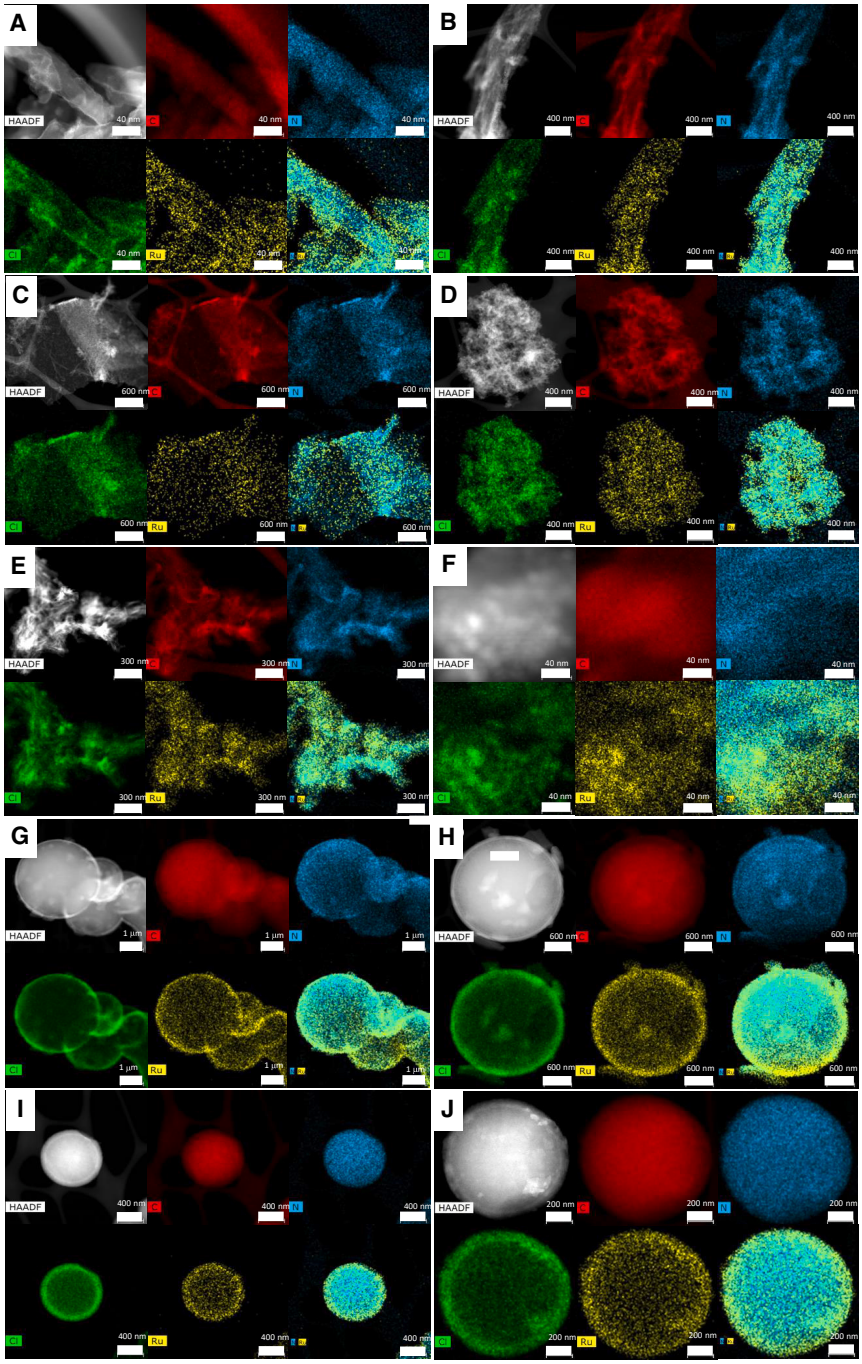

Figure 2. HAADF and EDS of the COFs before and after reaction

(A) Ru 10% Tp Pa-1. Scale bars, 40 nm.
(B) Ru 10% Tp Pa-1 used (scale bar, 400 nm).
(C) Ru 10% Tp o-tolidine (scale bar, 600 nm).
(D) Ru 10% Tp o-tolidine used (scale bar, 400 nm).
(E) Ru 10% TFB Hz (scale bar, 300 nm).
(F) Ru 10% TFB Hz used (scale bar, 40 nm).
(G) Ru 10% TFB o-tolidine (scale bar, 1 µm).
(H) Ru 10% TFB o-tolidine used (scale bar, 600 nm).
(I) Ru 10% TFB TAB (scale bar, 400 nm).
(J) Ru 10% TFB TAB used (scale bar, 200 nm)

The Ru/COF catalysts were characterized by ATR-FTIR (Figure S4). In comparison with original COF, all characteristic peaks were preserved in fresh and spent Ru/COF. After the $RuCl_3$ impregnation, the FTIR bands at around 3,210 and 3,415 cm^{-1} corresponding to the N—H stretching mode[37,38] lose their intensity, which could indicate their interaction with the introduced ruthenium species.[38] The interaction between Ru and N-H groups seems to increase in the samples after the reaction. Note that a new FTIR band around 1,940 cm^{-1} appears that could be assigned to the Ru—H stretching vibrations. This suggests that the Cl anions in the Ru coordination environment (from $RuCl_3$) have been replaced by hydride and N-H ligands.[39]

The metal dispersion in COFs was examined by HAADF-STEM and STEM-energy-dispersive X-ray spectroscopy (EDS) (Figures 2 and S2). STEM and EDS images did not reveal distinct Ru nanoparticles in the samples after impregnation, indicating high ruthenium dispersion. The Ru chemical maps overlap with the chemical maps of chlorine. This suggests that Ru could be mostly present in the form of chlorine-containing species even in the samples containing up to 9.5 wt. % Ru. This observation is consistent with a high chlorine content measured in the fresh Ru/COF catalysts (Table S1). The samples with larger spherical COF particles showed some enrichment of the surface layer with ruthenium. The formation of core-shell structures can be due to slow diffusion of ruthenium cations inside larger COF particles during the impregnation with $RuCl_3$.

Interestingly, even after the reaction, no ruthenium clusters or agglomerates were observed in the catalysts. According to STEM analysis, all spent Ru-COF catalysts exhibit uniform ruthenium dispersion with particles smaller than 1 nm. Thus, no ruthenium sintering and formation of metallic ruthenium particles were observed by STEM. It's important to emphasize that ruthenium nanoparticles were not detected by TEM in the fresh catalysts. We assume that Ru is mostly present in COF as single-atom species. The suggestion regarding the presence of single Ru atoms in COF was further confirmed below through X-ray absorption near edge strucure (XANES) and extended X-ray absorption fine structure (EXAFS) data. This gives a density of ruthenium single-atom sites for Ru10% Tp *p*-phenylenediamine (Pa-1) and Ru10% TFB o-Tol higher than 1 atom/nm^2 (Table 1).

Further information about Ru species in the fresh and spent catalysts was obtained using X-ray photoelectron spectroscopy (XPS) and X-ray absorption. The Ru 3d and 3p XPS spectra of Ru/COF fresh and spent catalysts are shown in Figure 3. In the Ru/COF catalysts, the Ru 3d and Ru 3p XPS binding energies (BEs) are 2 eV higher relative to metallic Ru in fresh and spent catalysts (Tables S3 and S4). This is indicative of Ru-oxidized state and absence of Ru metallic phase. In the Tp Pa-1 sample, Ru BEs are close to those measured for Ru acetylacetonate. It seems that in Ru/COFs, the ruthenium species can be coordinated by the C=O groups of Tp-derived COFs. For TFB-derived COFs, BEs are closer to the values of RuO_2 and 1 eV lower than in $RuCl_3$. The XPS atomic concentrations are given in Tables S3 and S4, respectively, for the fresh and spend catalysts. For all the samples, chlorine disappears after the reaction and has been replaced by another ligand in the Ru coordination.

FTIR spectroscopy further validated the existence of single-atom ruthenium sites. The Ru-containing COF were dark, which complicated measuring IR spectra. Nevertheless, the IR spectra of carbon monoxide adsorbed on Ru10% TPB 1,3,5-tris(4-aminophenyl)benzene (TAB) (Figure S7) exhibit a peak at 2,045 cm^{-1}, which was assigned to the CO complexes with isolated Ru species. Heating the sample in

Table 1. Catalytic results for the CO_2 hydrogenation to formic acid

Sample	Reactions conditions	mg	Single-site density, Ru nm^{-2}	mg_{HCOOH} $g_{catalyst}^{-1}$ h^{-1}	TOF h^{-1}
Ru10% Tp Pa-1	90°C/15 h 20 bar H_2 20 bar CO_2	35	1.14	5.0	5.3
Ru10% Tp *o*-Tol		56	0.39	8.1	9.8
Ru10% TFB Hz		112	0.24	16.2	34
Ru10% TFB *o*-Tol		42	1.66	6.1	13
Ru10% TFB TAB		111	0.64	16.1	49
Ru10% Tp Pa-1	120°C/1 h 30 bar H_2 10 bar CO_2	33	1.14	71.4	76
Ru10% Tp *o*-Tol		37	0.39	80.9	98
Ru10% TFB Hz		53	0.24	116.0	243
Ru10% TFB *o*-Tol		29	1.66	63.2	140
Ru10% TFB TAB		34	0.64	73.6	222

The values of formic acid in milligrams were obtained using ^{1}H NMR liquid state; relevant calculations are available in the supplemental information.

vacuum resulted in progressive decrease in the intensity of this band. Interestingly, no shift in the position of this band was observed, which is consistent with the absence of CO-CO dipole interaction when adsorbing on a single ruthenium site. At the same time, a new IR band appears at 2,011 cm^{-1} after sample heating in vacuum. This peak could be assigned to partial reduction of ruthenium occurring during the sample heating at higher temperatures.

Catalytic performance in the CO_2 hydrogenation to formic acid

The CO_2 hydrogenation tests were conducted in aqueous phase in the autoclave at the total pressure of 40 bar at 90°C and 120°C with H_2/CO_2 ratios of 1 and 3. In all the experiments, the same amount of Ru was loaded in the reactor. The synthesis of formic acid is limited by the thermodynamics; 1.3 M triethylamine (TEA) was added to increase the equilibrium conversion. In addition, it was shown[9] that the presence of a stronger base such as TEA can reduce the reaction activation barrier. TEA forms a complex[40] with formic acid, which can be used as liquid reducing agent in many selective reductions.

Low CO_2 conversions were observed with $RuCl_3$ and $Ru(OH)_3$ as catalysts, while the Ru/COF catalysts exhibited higher activity (Table 1). Only formic acid was detected as a product; no CO, methane, or methanol were observed by gas chromatography or ^{1}H NMR. The overall catalytic activity was evaluated on the weight basis, which corresponds to the amount of CO_2 converted to formic acid per gram of catalyst and as turnover frequency, assuming that only Ru provides active sites for the reaction. The highest activity at both 90°C and 120°C was observed over Ru10% TFB Hz Ru10% TFB TAB, while Ru10% Tp Pa-1 and Ru10% Tp o-Tol exhibited the lowest activity. The weight-based catalytic activity is of paramount importance for the practical application of a catalyst. It is worth noting that the catalysts developed in this work, especially Ru10% TFB Hz, exhibited the highest weight-based activity when compared to previously reported data summarized in Table S6 and relevant references.

Remarkably, no discernible relation exists between the intrinsic activity of Ru catalysts expressed as turnover frequency (TOF) and their overall surface area (Table S2). The surface area of COF is composed of 2D layers. Variations in the arrangement of these layers, leading to distinct surface areas, can be modified through pre-treatment and reaction conditions. Figure S8 presents the activity of Ru/COF after conducting several reaction cycles. Important, Ru10% TFB *o*-Tol shows unchangeable activity after several cycles.

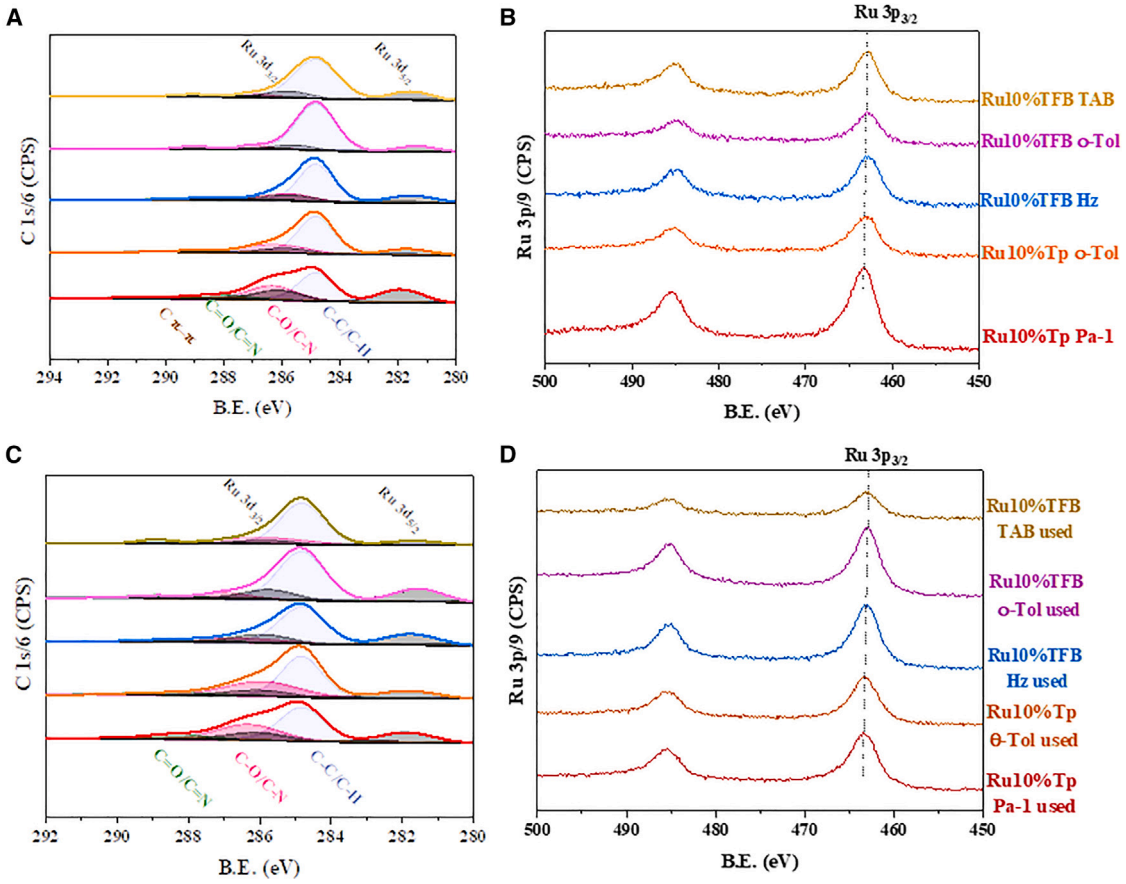

Figure 3. XPS spectra of fresh and spent Ru/COF catalysts

(A) Ru 3d XPS spectra of fresh catalysts.

(B) Ru 3p XPS spectra of fresh catalysts.

(C) Ru 3d XPS spectra of spent catalysts.

(D) Ru 3p XPS spectra of spent catalysts.

Ex situ and *in situ* X-ray absorption (XAS) investigation of ruthenium catalysts

Figures S9 and S10A display the Ru K-edge *ex situ* XANES spectra of reference compounds and fresh Ru/COF catalysts, respectively. The XANES spectra of fresh Ru/COF catalysts are rather similar and strongly reassemble those of $RuCl_3$ and $RuCl_3(NH_3)_6$. This observation is consistent with a large amount of chlorine detected in the catalysts by XRF. To order to evaluate the concentration of different phases in the fresh and used catalysts, the XANES spectra (Figure S10) were fitted separately. The results of linear combination fitting of XANES spectra using ruthenium hydroxide, ruthenium trichloride, hexaammineruthenium trichloride, ruthenium oxide, and metallic ruthenium for the fresh and spent catalysts are displayed in Table S7. The fits are shown in Figure S12. All the fresh catalysts present the majority of Ru species as $RuCl_3$ and/or Ru-N complexes, here represented by reference $RuCl_3(NH_3)_6$. The Ru10% TFB Hz and Ru10% TFB TAB fresh catalysts have the lower fraction of metallic Ru, ~11% and ~16%, respectively. Metallic Ru in the fresh catalysts can be possibly produced by reduction of ruthenium species by the COF matrix during the catalyst drying. Notably, these are the most active catalysts (see Table 1). The XANES spectra of Ru/COF change after the catalytic reaction (Figure S10A). For the most stable catalyst, Ru10% TFB o-Tol, the majority of Ru species in the spent catalyst correspond to Ru hydroxide type species. Also, the fraction of metallic Ru does

not change in comparison with the fresh counterpart and remains around 25%. This behavior was not observed for the other catalysts. No contribution of Ru chloride to XANES was detected, consistent with chlorine removal from the catalyst during the reaction.

Figure S11A shows the Fourier transform (FT) EXAFS moduli of the fresh catalysts (without phase shift). The fresh Ru/COF catalysts exhibit a broad intense peak at 1.8–1.9 Å. A similar peak was also observed in the FT EXAFS of $RuCl_3$. This suggests that this peak may be related to Ru-Cl coordination in the first Ru coordination shell. Interestingly, the FT moduli of EXAFS in the Ru/COF catalysts do not show a second peak at 3.35 Å, which was observed for $RuCl_3$. The absence of distinct second coordination shell of $RuCl_3$ in the fresh Ru/COF samples suggests low crystallinity of Ru chloride and possible formation of isolated Ru species. Note that some fraction of Ru metallic phases was detected in the samples from the results of XANES linear combination fitting.

In the spent catalysts (Figure S11B), the FT EXAFS moduli show an intense broad peak at 1.6–1.7 Å. The position of this peak is similar to that of the Ru-O coordination in Ru hydroxide, Ru oxide, and Ru-N complexes species, and it is shifted from the position of Ru-Cl peak in $RuCl_3$. In addition, a new intense peak at 2.3 Å appears in the FT EXAFS. This peak seems to be related to the Ru-Ru coordination in metallic Ru and is indicative of the partial sintering of Ru single atoms into metallic nanoparticles. Interestingly, among the spent Ru/COF catalysts, the Ru-Ru coordination number is smaller in the Ru10% TFP *o*-Tol, which could correspond to a smaller number of metallic Ru atoms in the coordination shell of Ru and a lower extent of Ru reduction in this sample. This is consistent with the assumption that single-atom metal species have higher contribution to the CO_2 hydrogenation to formic acid than ruthenium metal nanoparticles.

In order to provide further insights into the evolution of catalyst structure during the reaction, we performed *operando* XAS measurements of Ru10% TFB o-Tol and Ru10% TFB TAB at Ru K-absorption edge under the flow of H_2 and CO_2 (H_2/CO = 1) at 100°C (Figure 4). The evolution of XANES spectra during the reaction was different for the two samples. The XANES spectra of Ru10% TFB o-Tol (Figure 4A) show evolution of the Ru K-absorption edge from Ru chloride to that which is more characteristic of Ru hydroxide and Ru-N complexes.

At the same time, the XANES spectra of Ru10% TFB TAB (Figure 4B) show a steady decrease in the intensity of white line, which corresponds to the increase in the fraction of metallic phase and correspondingly ruthenium reduction. Note that Ru10% TFB *o*-Tol showed stable performance in the CO_2 hydrogenation to formic acid for several cycles, while Ru10% TFB TAB exhibited a major deactivation (Figure S8).

The phase composition of Ru catalysts during the reaction was calculated from fitting the *operando* XANES spectra of Ru10% TFB *o*-Tol and Ru10% TFB TAB using the spectra of reference compounds (Figures 5A and 5B). In Ru10% COF TFB *o*-Tol, the amounts of RuN complexes and Ru hydroxide species increase under the reaction conditions, while the concentration of metallic Ru phases decreases. This observation suggests the redispersion of Ru species and increased interaction of Ru complexes with N species in the COF during the reaction. In contrast, the reaction results in progressive increase in the amount of metallic ruthenium in Ru10% TFB TAB (Figure 5B).

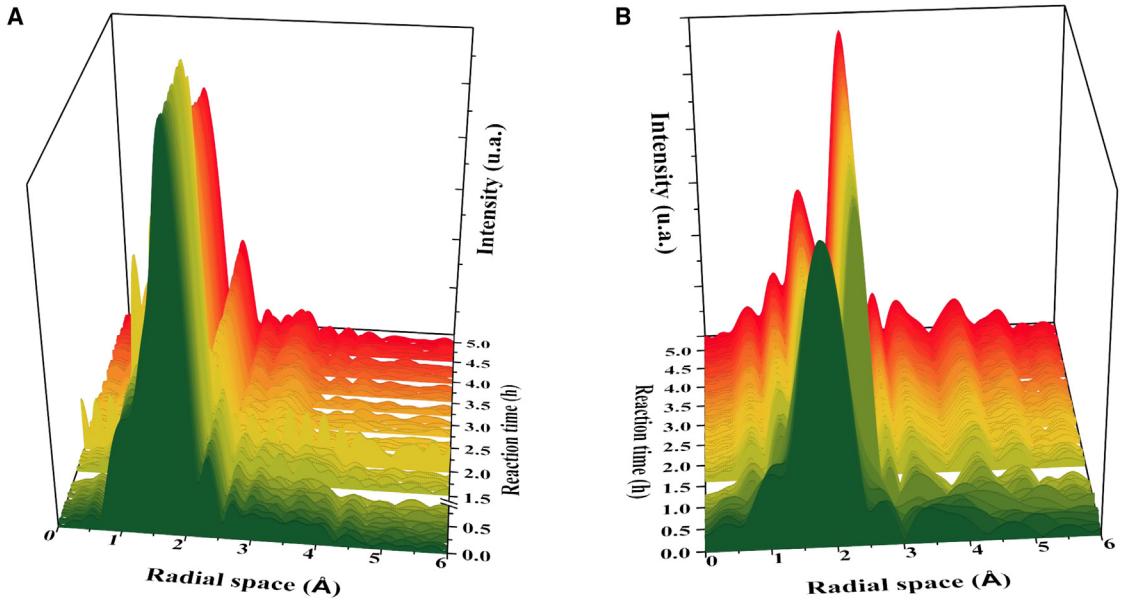

Figure 4. Evolution of *in situ* XAS spectra during the CO_2 hydrogenation
(A) Ru10% TFB *o*-Tol.
(B) Ru10% TFB TAB.

The liquid samples collected during *operando* XAS experiments were analyzed by ^{1}H NMR. The amount of produced formic acid was 0.062 mmol for Ru10% TFB TAB and 0.022 mmol for Ru10% TFB *o*-Tol. This corresponds respectively to turnover numbers (TONs) of 24.6 and 3.2 for Ru10% TPB TAB and Ru10% TPB *o*-Tol. Note that, similar to the batch reaction tests, Ru10% TFB TAB exhibited higher activity than Ru10% TFB *o*-Tol. Some difference in absolute TON values may be due to different operating conditions in *operando* XAS experiments conducted in a flow reactor and in conventional batch catalytic tests.

Structure-performance correlations and stability of ruthenium catalysts supported by COF

A wide range of characterization techniques employed in this work is indicative of the presence of isolated single-atom ruthenium species in COF catalysts, making COFs a suitable matrix for achieving highly dispersed ruthenium species. Previous reports suggest[41] that COFs can be considered as excellent nanoreactors for CO_2 capture and *in situ* conversion. The mechanistic aspects of CO_2 hydrogenation over Ru SACs are investigated in our previous publication.[9] It was shown that hydrogen dissociated heterolytically on single-atom catalysts with no change in the formal oxidation state of the metal center. Once the catalytic active species, the Ru-H, is formed, the reaction follows 4 steps: CO_2 addition, formate synthesis, hydrogen activation, and release of the formate with the aid of a strong base followed by concurrent regeneration of the active species.

First, let's discuss how the COF structure influences the catalytic performance of ruthenium catalysts in the hydrogenation of CO_2 to formic acid. Our experimental data suggest that at the same Ru content, the COF chemical composition determines to a larger extent the fraction of isolated single-atom ruthenium species. Palkovits et al.[42] recently reported a lower CO_2 hydrogenation rate using iridium single-site catalysts, which was linked to a decrease in the dispersion of iridium.

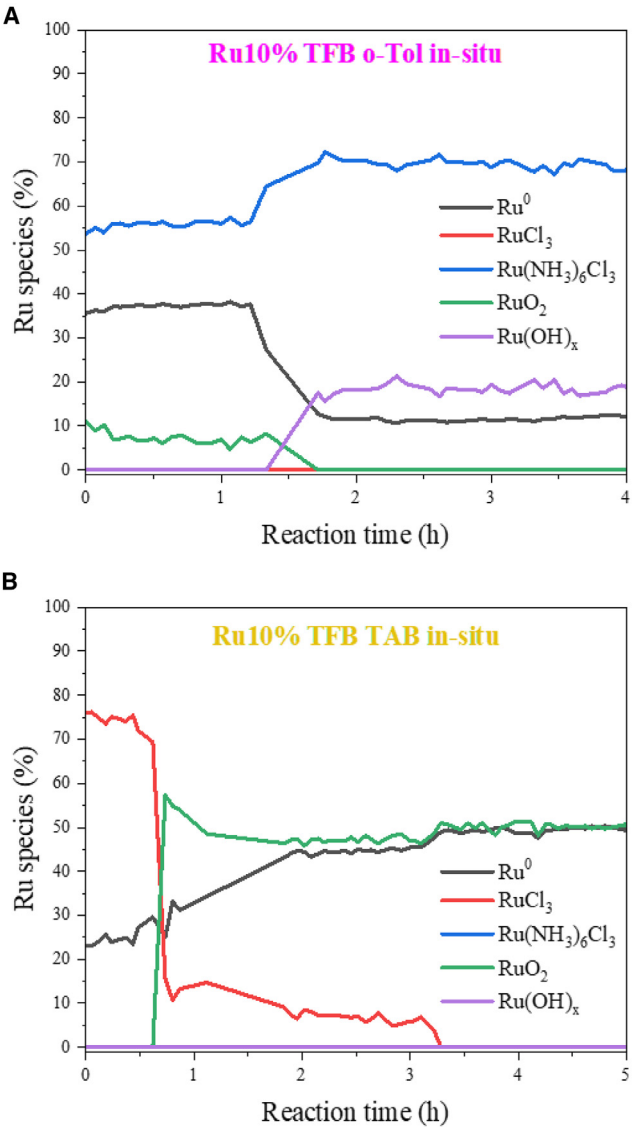

Figure 5. Evolution of catalyst phase composition during the CO_2 hydrogenation

The phase percentages were calculated from LC XAS.

(A) Ru10% TFB *o*-Tol.

(B) Ru10% TFB TAB.

The overall reaction rate depends on the number of active sites and their intrinsic catalytic performance, often expressed as TOF. An increase in the density of ruthenium single-atom sites, along with an improvement in their TOF, can contribute significantly to designing highly active catalysts. On the one hand, COFs enable ruthenium catalysts with extremely high densities of single-atom sites (Table 1; Table S6). On the other hand, multiple factors may influence the intrinsic activity of a catalyst, such as interactions between the support and metal, and mass transfer of reactants/products. Since the highest activity was observed on the samples without carbonyl groups, we assume that the contribution of the Ru species coordinated by C=O and C-OH groups to the reaction is not very significant. Our results clearly show that the intrinsic catalytic activity (TOF) is strongly affected by the amount of nitrogen in the catalysts (Figure 6). Moreover, the intrinsic catalytic activity

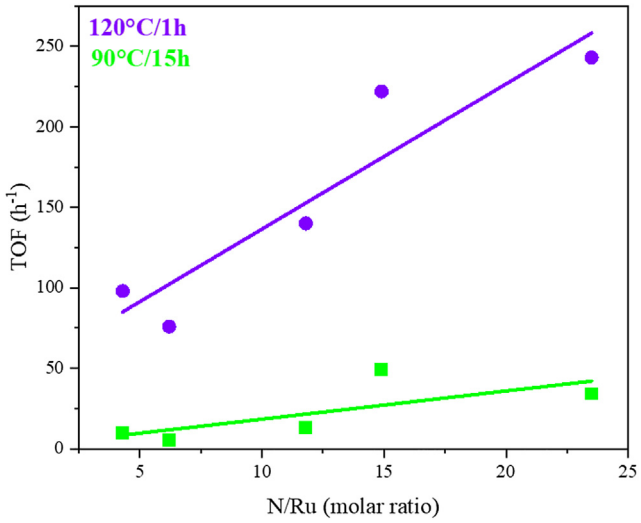

Figure 6. TOFs measured on the Ru/COF catalysts at 90°C and 120°C as functions of N/Ru experimental molar ratio

Data were sourced from Table 1.

of Ru catalysts is almost proportional to the N/Ru ratio in the catalysts. In agreement with the characterization results, this observation underscores the crucial role of nitrogen-containing groups in contributing to the intrinsic activity.

Importantly, COFs have a very high capacity to stabilize isolated single-site ruthenium atoms, even at relatively high ruthenium content. This results in an extremely high weight-based activity of the prepared Ru/COF catalyst compared to previous results from the literature (Tables 1 and S6). Besides anchoring Ru single metal atoms, nitrogen functional groups in the COF may also play a role in CO_2 hydrogenation, for example, by potentially facilitating CO_2 adsorption. In the present work, the highest activity has been achieved in Ru10% TFB Hz, which has the highest density of ruthenium sites and their high intrinsic activity, due to a higher fraction of nitrogen in the framework.

Stability of the single-metal ruthenium species during the reaction is another issue that can determine the long-term catalyst productivity. The most active Ru10% TFB TAB and TFB Hz lose their activity in the second and third reaction cycles (Figure S9), while Ru10% TFB *o*-Tol maintains its catalytic activity. The characterization of the spent catalysts showed partial reduction of Ru oxidized species to metal state in most of catalysts, which results in the appearance of a peak of Ru-Ru coordination in FT EXAFS modulus at 2.3 Å (Figure S11B). Higher intensity of the FT EXAFS peak attributed to the Ru-Ru coordination shell and higher extent of Ru reduction was observed in less stable Ru10% TFB TAB and Ru10% TFB Hz catalysts. The reduction of ruthenium resulted in a decrease in the concentration of Ru single-atom sites. This reduction was less significant for the Ru10% TFB *o*-Tol catalyst. Ruthenium metallic nanoparticles have therefore a much lower efficiency in CO_2 hydrogenation to formic acid compared to ruthenium single-atom species.

Operando XAS experiments have given crucial information about the evolution of Ru phases in the COF-supported Ru10% TFB TAB and Ru10% TFB *o*-Tol catalysts during the reaction. Ru species in Ru10% TFB TAB underwent gradual reduction to metallic phase during the first 2–3 h of reaction in a flow reactor, while redispersion

and even possible re-oxidation of ruthenium species were detected in the Ru10% TFB *o*-Tol catalyst (Figure 5A). These experiments further confirm importance of Ru dispersion, stability of single-atom ruthenium species, and their intrinsic activity for obtaining highly active and productive catalysts for CO_2 hydrogenation to formic acid. The stability of the catalyst is a more complex parameter. Nitrogen density may affect the catalyst stability. Because deactivation proceeds via reduction, other factors should be considered, such as the distance between single-atom ruthenium sites and steric hindrances (e.g., presence of vicinal CH_3 groups), which may slow to some extent migration of single ruthenium atoms and their sintering into metallic nanoclusters.

Deposition of ruthenium via impregnation over the COF materials results in a large fraction of ruthenium single-atom species. In the fresh catalysts, Ru is coordinated by chlorine and located in a close interaction with nitrogen-containing groups of COFs. The chlorine atoms are removed from the catalysts during the CO_2 hydrogenation.

The catalytic performance of ruthenium catalysts supported over COF materials is strongly affected by the COF structure. Because of COFs' remarkable ability to stabilize isolated single-atom ruthenium sites at high ruthenium content, coupled with their intrinsic activity, we have attained an exceptionally high CO_2 hydrogenation rate at lower reaction temperatures compared to previous findings. While various catalyst parameters can influence catalytic performance, it was observed that the intrinsic rate of CO_2 hydrogenation exhibited a nearly proportional relationship with the density of nitrogen species in the COF framework. No effect of oxygen-containing functional groups on ruthenium dispersion was observed. The stability of catalysts was related to the hindered reducibility of ruthenium single atoms during the reaction. The proposed strategy can be extended for the design of numerous SAC metal catalysts supported by COF for different reactions.

EXPERIMENTAL PROCEDURES

Resource availability

Lead contact

Further information and requests for resources should be directed to and will be fulfilled by the lead contact, Andrei Khodakov (andrei.khodakov@univ-lille.fr).

Materials availability

This study did not generate new unique materials.

Data and code availability

The data that support the findings in this study are available from the article and its supplemental information. All other relevant data are available from the lead contact upon reasonable request.

Materials

The following materials were used: Tp (Sigma-Aldrich); TFB (TCI products); Hz (Sigma-Aldrich); Pa-1; *o*-Tol (Sigma-Aldrich); TAB (TCI products); methanol (Sigma-Aldrich); tetrahydrofuran (Sigma-Aldrich); acetone; 1,4-dioxane (Sigma-Aldrich), acetic acid (Sigma-Aldrich); mesitylene (Sigma-Aldrich); dichloromethane; triethylamine (Sigma-Aldrich); $RuCl_3 \cdot H_2O$ (Sigma-Aldrich).

Catalyst preparation

The COF synthetic procedures are described in the supplemental information. All the Ru/COF catalysts were then prepared by wetness impregnation of synthetized

COF using a solution of ruthenium chloride in methanol/water mixture (v/v = 1/1) followed by evaporation in oil bath at 80°C in a fume hood and then drying in oven at 80°C for 2 h.

Catalyst characterization

The nitrogen physisorption measurements were carried out using a Micromeritics Tristar 3020 surface area and porosimetry analyzer. Prior to the N_2 adsorption, the sample was degassed at 150°C for 12 h. The N_2 adsorption-desorption isotherms were measured at −196°C. The BET surface area was determined using the data points in the pressure range of 0.05–0.3 P/P_0 from the N_2 adsorption isotherms at −196°C.

An X-ray Diffractometer Smart Lab Guidance Rigaku, 200 mA, 45 kV (9 kW), with Cu $K\alpha_1$ radiation (λ = 0.15406 nm), rotating anode, parallel beam, was used for the XRD measurements. The XRD patterns were collected in the 2°−40° (2θ) range, with a 0.01° step size and 0.07 s step time.

The TEM and EDS measurements were done using an FEI Tecnai G2 and a Thermo Fisher Titan Themis microscope, operating at 200 and 300 kV, respectively. The sample was deposited onto a 400-mesh carbon-coated copper grid.

To determine the thermal stability of the samples, the thermogravimetric analysis was performed using an SDT Q600 V20.9 Build 20 TGA and differential scanning calorimeter with 2.5 mg of sample. The temperature ramp was 10°C/min up to 800°C under N_2 (100 mL min^{-1}). Also, TGA was carried out by SDT Q600, using 5 mg of sample, under air conditions (100 mL min^{-1}), at the heating rate of 10° min^{-1} from 50°C to 900°C.

A Nicolet iS50 FTIR spectrometer (Thermo Scientific) equipped with a DTGS-ATR detector, a diamond ATR window, a KBr beam splitter for the range of 4,000–525 cm^{-1}, and a solid substrate beam splitter for the range of 1,800–80 cm^{-1}, scan number of 128 cm^{-1}, respectively, and resolution of 2 cm^{-1}, was used for the IR analysis.

The nuclear magnetic resonance, solid state, was carried out on a Bruker Avance III 400-MHz spectrometer, equipped with 4-mm standard probe for ^{1}H and ^{13}C, DEPTH, and CPMAS, Ro = 12.5 kHz and 100.6 MHz, respectively, and the chemical shifts for protons are reported in parts per million (ppm). For the analysis of catalytic results, the NMR in liquid state was performed in the 300-MHz Bruker AVANCE III HD spectrometer, equipped with a BBFO 5-mm probe, a gradient Z, and a sample changer Xpress 60 for 5-mm tubes.

A Kratos Axis Ultra DLD spectrometer, equipped with a monochromatized Al Ka X-ray source (1,486.6 eV) operating at 180 W, was used for the XPS measurements. The pass energy used to record all the core level spectra of C 1s, O 1s, N 1s, and Ru 3p was 40 eV. The correction of the BEs was done with respect to C 1s fixed at 284.6 eV. The Shirley-type background was used in each spectrum to calculate the relative surface atomic concentrations.

The XRF measurements were performed with an energy-dispersive micro-X-ray fluorescence spectrometer M4 TORNADO (Bruker), equipped with 2 anodes, a rhodium X-ray tube 50 kV/600 mA (30 W), and a tungsten X-ray tube 50 kV/700 mA (35 W). The detector used is a Silicon-Drift-Detector Si (Li) with <145 eV resolution at 100,000 cps (Mn Ka). For

each sample, in which 36 points within an area with a diameter of 200 μm were analyzed, all the measurements were done under vacuum (20 mbar).

The *ex situ* X-ray absorption spectra were recorded at the XAFS beamline station of the Elettra Sincrotrone (Trieste, Italy)[43] and SuperXAS beamline in Swiss Light Source (SLS, Villigen, Switzerland). In Elettra, the X-ray beam was vertically collimated silicon ingot with Pt-coated mirror positioned at 3.0 mrad with respect to the direct beam. The beam was monochromatized by a fixed-exit double-cam double-crystal monochromator, using a pair of Si (111) crystals. The monochromatic beam that has a fixed height of 1.2 mm vertically and horizontally variable according to the size of the sample inside the capillary. The beam energy was calibrated using metallic Ru (K edge at 22,117 eV). In the SLS synchrotron, the incident photon beam was selected by a Si (111) channel-cut monochromator from the polychromatic beam coming from a 2.9-T superbend magnet. The rejection of higher harmonics and the collimation were achieved by a platinum-coated collimating mirror at 2.5 mrad located before the monochromator, while focusing was achieved by a platinum-coated toroidal mirror at 2.5 mrad. For the detection of Ru K-edge XAS, we calibrated the beamline using metallic Ru (K edge at 22,117 eV). The samples were measured in transmission mode using 15-cm-long ionization chambers filled with 1 bar of Ar and 1 bar of N_2. The size of the X-ray beam on the sample was about 1.5 mm in horizontal and 0.5 mm in vertical directions.

The *in situ* Ru K-edge X-ray absorption spectra during the CO_2 hydrogenation were measured at beamline CLÆSS of the ALBA synchrotron (Barcelona, Spain). The X-ray energy range at Ru K-absorption edge was covered, using pairs of Si(111) and Si(311) crystals. Beam intensity before (I0) and after (I1) the sample was measured by ionization chambers. The current signals from the ionization chambers were collected, amplified, and converted to output voltage by the ALBA Electrometer. Higher harmonics were cut by collimating mirrors located after the monochromator. The third ionization chamber was used to simultaneously measure the intensity I3 after the reference ruthenium foil for energy calibration.

The schema of *in situ* experimental setup is given in Figure S13. For the *in situ* XANES and EXAFS measurements, the sample was loaded in a 2-mm quartz capillary. The XAS measurements at Ru K edge were performed in the flow of aqueous solution of triethylamine (TEA), which was used as formic acid scavenger. The aqueous solution was added to the capillary using a syringe pump. The measurements were performed in a gas flow of He (p = 10 bar) and in a flow of H_2/CO = 3 mixture (p = 10 Bar) at temperatures ranging from ambient to 120°C. The liquid samples downstream of the capillary were collected and analyzed by ^{1}H NMR for the presence of formic acid. For the NMR analysis, the samples (0.5 mL) were mixed with 0.1 mL solution DMSO in D_2O (1:2,000 vol).

XAS data processing included energy calibration, normalization, background removal, and first-shell Fourier analysis. All obtained XAS data were analyzed using the Demeter software package.[44] Because XAS experiments were performed in different synchrotron facilities, the pre-treatment and processing parameters vary according to the output file. Typically, normalization is performed considering a regressed line on the pre-edge region and a polynomial (quadratic or cubic, depending on the data) on the post-edge region. To perform EXAFS extraction, the AUTOBK algorithm implemented on the Demeter package is used. FT of the EXAFS is obtained by choosing a proper range (a Hanning window) on k-space that depends on the signal-to-noise ratio of the dataset, but it typically lies between 3.0 and 14.0 in k-space.

Catalytic tests

The CO_2 hydrogenation to formic acid was performed in a 40-mL stainless-steel autoclave batch reactor equipped with a pressure gauge. For the reaction, 10 mg of catalyst was added to the reactor with 6 g of water and 0.9 g of TEA. The reactor was then sealed and pressurized to 40 bar with CO_2 and H_2 (CO_2/H_2 = 1:1 or 1:3) and subjected in the heating plate to stirring during the reaction time (1 h or 15 h) at 90°C or 120°C. After cooling to room temperature, the pressure was released, and the reacted solution was filtered and collected to analyze the product concentration by ^1H NMR, using as internal standards the signals from water and TEA. The gaseous phase was analyzed using gas chromatography. No CO or methane was detected.

SUPPLEMENTAL INFORMATION

Supplemental information can be found online at https://doi.org/10.1016/j.xcrp.2024.101926.

ACKNOWLEDGMENTS

The authors thank Dr Joëlle Thuriot, Johann Jezequel, Laurence Burylo, and Jean-Charles Morin for the help with elementary analysis, XRF, BET, XRD, and ATR-FTIR measurements. The authors are thankful to I-SITE Université Lille Nord-Europe (Nanoconfinement project) for the financial support. The ALBA, SLS, and Elettra synchrotrons are acknowledged for the use of beamtime.

AUTHOR CONTRIBUTIONS

A.K.F., G. J., and A.Y.K. conceived the idea of the work. A.K.F., G.J., and A.A. performed microscopy measurements and analysis. S.A.C., Y.Z., and M.C. performed the *in situ* and operando experiments. D.O.S., O.V.S., and V.M.-D. performed XAS analysis. V.V.O. contributed to the catalytic tests and their interpretation. A.K.F. designed the experiments and analyzed the data. A.K.F., G.J., and A.Y.K. wrote the manuscript. All authors reviewed the manuscript and agreed on its content.

DECLARATION OF INTERESTS

The authors declare no competing interests.

Received: December 3, 2023
Revised: February 3, 2024
Accepted: March 18, 2024
Published: April 8, 2024

REFERENCES

1. Côté, A.P., Benin, A.I., Ockwig, N.W., O'Keeffe, M., Matzger, A.J., and Yaghi, O.M. (2005). Porous, Crystalline, Covalent Organic Frameworks. Science *310*, 1166–1170. https://doi.org/10.1126/science.1120411.

2. Geng, K., He, T., Liu, R., Dalapati, S., Tan, K.T., Li, Z., Tao, S., Gong, Y., Jiang, Q., and Jiang, D. (2020). Covalent Organic Frameworks: Design, Synthesis, and Functions. Chem. Rev. *120*, 8814–8933. https://doi.org/10.1021/acs.chemrev.9b00550.

3. Fang, Q., Gu, S., Zheng, J., Zhuang, Z., Qiu, S., and Yan, Y. (2014). 3D microporous base-functionalized covalent organic frameworks for size-selective catalysis. Angew. Chemie - Int. Ed. *53*, 2878–2882. https://doi.org/10.1002/anie.201310500.

4. Qiao, B., Wang, A., Yang, X., Allard, L.F., Jiang, Z., Cui, Y., Liu, J., Li, J., and Zhang, T. (2011). Single-atom catalysis of CO oxidation using Pt_1/FeO_x. Nat. Chem. *3*, 634–641. https://doi.org/10.1038/nchem.1095.

5. Yang, X.-F., Wang, A., Qiao, B., Li, J., Liu, J., and Zhang, T. (2013). Single-Atom Catalysts: A New Frontier in Heterogeneous Catalysis. Acc. Chem. Res. *46*, 1740–1748. https://doi.org/10.1021/ar300361m.

6. Liu, L., and Corma, A. (2018). Metal Catalysts for Heterogeneous Catalysis: From Single Atoms to Nanoclusters and Nanoparticles. Chem. Rev. *118*, 4981–5079. https://doi.org/10.1021/acs.chemrev.7b00776.

7. Zhuang, J., and Wang, D. (2023). Recent advances of single-atom alloy catalyst: Properties, synthetic methods and electrocatalytic applications. Mater. Today Catal *2*, 100009. https://doi.org/10.1016/j.mtcata.2023.100009.

8. Ma, M., Gong, C., An, X., Shi, Z., Liu, Z., and He, Y. (2023). The emergence of single-atom-layer catalysis. Mater. Today Catal *1*, 100004. https://doi.org/10.1016/j.mtcata.2023.100004.

9. Wang, Q., Santos, S., Urbina-Blanco, C.A., Hernández, W.Y., Impéror-Clerc, M., Vovk, E.I.,

Marinova, M., Ersen, O., Baaziz, W., Safonova, O.V., et al. (2021). Solid micellar Ru single-atom catalysts for the water-free hydrogenation of CO_2 to formic acid. Appl. Catal. B Environ. *290*. 120036-9. https://doi.org/10.1016/j.apcatb.2021.120036.

10. Iemhoff, A., Vennewald, M., and Palkovits, R. (2023). Single-Atom Catalysts on Covalent Triazine Frameworks: at the Crossroad between Homogeneous and Heterogeneous Catalysis. Angew. Chemie Int. Ed. *62*. https://doi.org/10.1002/anie.202212015.

11. Luo, T., Gilmanova, L., and Kaskel, S. (2023). Advances of MOFs and COFs for photocatalytic CO_2 reduction, H_2 evolution and organic redox transformations. Coord. Chem. Rev. *490*, 215210. https://doi.org/10.1016/j.ccr.2023.215210.

12. Liu, J. (2017). Catalysis by Supported Single Metal Atoms. ACS Catal. *7*, 34–59. https://doi.org/10.1021/acscatal.6b01534.

13. Thomas, J.M., Raja, R., and Lewis, D.W. (2005). Single-Site Heterogeneous Catalysts. Angew. Chemie Int. Ed. *44*, 6456–6482. https://doi.org/10.1002/anie.200462473.

14. Gates, B.C., Flytzani-Stephanopoulos, M., Dixon, D.A., and Katz, A. (2017). Atomically dispersed supported metal catalysts: perspectives and suggestions for future research. Catal. Sci. Technol. *7*, 4259–4275. https://doi.org/10.1039/C7CY00881C.

15. Petrov, A.W., Ferri, D., Krumeich, F., Nachtegaal, M., van Bokhoven, J.A., and Kröcher, O. (2018). Stable complete methane oxidation over palladium based zeolite catalysts. Nat. Commun. *9*, 2545. https://doi.org/10.1038/s41467-018-04748-x.

16. Wang, D., Li, Q., Han, C., Xing, Z., and Yang, X. (2019). Single-atom ruthenium based catalyst for enhanced hydrogen evolution. Appl. Catal. B Environ. *249*, 91–97. https://doi.org/10.1016/j.apcatb.2019.02.059.

17. Li, Z., Yang, Y., Wang, S., Gu, L., and Shao, S. (2021). High-Density Ruthenium Single Atoms Anchored on Oxygen-Vacancy-Rich g-C_3N_4-C-TiO_2 Heterostructural Nanosphere for Efficient Electrocatalytic Hydrogen Evolution Reaction. ACS Appl. Mater. Interfaces *13*, 46608–46619. https://doi.org/10.1021/acsami.1c12494.

18. Zhao, R., Wang, T., Li, J., Shi, Y., Hou, M., Yang, Y., Zhang, Z., and Lei, S. (2023). Two-dimensional covalent organic frameworks for electrocatalysis: Achievements, challenges, and opportunities. Nano Res. *16*, 8570–8595. https://doi.org/10.1007/s12274-022-5307-1.

19. Liu, S., Wang, M., He, Y., Cheng, Q., Qian, T., and Yan, C. (2023). Covalent organic frameworks towards photocatalytic applications: Design principles, achievements, and opportunities. Coord. Chem. Rev. *475*, 214882. https://doi.org/10.1016/j.ccr.2022.214882.

20. Li, T., Pan, Y., Shao, B., Zhang, X., Wu, T., He, Q., He, M., Ge, L., Zhou, L., Liu, S., et al. (2023). Covalent–Organic Framework (COF)-Core–Shell Composites: Classification, Synthesis, Properties, and Applications. Adv. Funct. Mater. *33*. https://doi.org/10.1002/adfm.202304990.

21. Lu, M., Zhang, M., Liu, J., Chen, Y., Liao, J., Yang, M., Cai, Y., Li, S., and Lan, Y. (2022). Covalent Organic Framework Based Functional Materials: Important Catalysts for Efficient CO_2 Utilization. Angew. Chemie Int. Ed. *61*. https://doi.org/10.1002/anie.202200003.

22. Hasija, V., Patial, S., Raizada, P., Aslam Parwaz Khan, A., Asiri, A.M., Van Le, Q., Nguyen, V.-H., and Singh, P. (2022). Covalent organic frameworks promoted single metal atom catalysis: Strategies and applications. Coord. Chem. Rev. *452*, 214298. https://doi.org/10.1016/j.ccr.2021.214298.

23. Cui, X., Gao, L., Ma, R., Wei, Z., Lu, C.-H., Li, Z., and Yang, Y. (2021). Pyrolysis-free covalent organic framework-based materials for efficient oxygen electrocatalysis. J. Mater. Chem. A *9*, 20985–21004. https://doi.org/10.1039/D1TA02795F.

24. Xu, Z., Deng, W., and Wang, X. (2021). 3D Hierarchical Carbon-Rich Micro-/Nanomaterials for Energy Storage and Catalysis. Electrochem. Energy Rev. *4*, 269–335. https://doi.org/10.1007/s41918-021-00094-7.

25. Ghosh, S., Molla, R.A., Kayal, U., Bhaumik, A., and Islam, S.M. (2019). Ag NPs decorated on a COF in the presence of DBU as an efficient catalytic system for the synthesis of tetramic acids via CO_2 fixation into propargylic amines at atmospheric pressure. Dalt. Trans. *48*, 4657–4666. https://doi.org/10.1039/C9DT00017H.

26. Das, S.K., Krishna Chandra, B., Molla, R.A., Sengupta, M., Islam, S.M., Majee, A., and Bhaumik, A. (2020). CuO grafted triazine functionalized covalent organic framework as an efficient catalyst for C-C homo coupling reaction. Mol. Catal. *480*, 110650. https://doi.org/10.1016/j.mcat.2019.110650.

27. Yang, X., Lan, X., Zhang, Y., Li, H., and Bai, G. (2023). Rational design of MoS_2@COF hybrid composites promoting C-C coupling for photocatalytic CO_2 reduction to ethane. Appl. Catal. B Environ. *325*, 122393. https://doi.org/10.1016/j.apcatb.2023.122393.

28. Matsubu, J.C., Yang, V.N., and Christopher, P. (2015). Isolated metal active site concentration and stability control catalytic CO_2 reduction selectivity. J. Am. Chem. Soc. *137*, 3076–3084. https://doi.org/10.1021/ja5128133.

29. Richard, A.R., and Fan, M. (2017). Low-Pressure Hydrogenation of CO_2 to CH_3OH Using Ni-In-Al/SiO2 Catalyst Synthesized via a Phyllosilicate Precursor. ACS Catal. *7*, 5679–5692. https://doi.org/10.1021/acscatal.7b00848.

30. Ou, M., Tu, W., Yin, S., Xing, W., Wu, S., Wang, H., Wan, S., Zhong, Q., and Xu, R. (2018). Amino-Assisted Anchoring of $CsPbBr_3$ Perovskite Quantum Dots on Porous g-C_3N_4 for Enhanced Photocatalytic CO_2 Reduction. Angew. Chemie *130*, 13758–13762. https://doi.org/10.1002/ange.201808930.

31. Lu, Q., and Jiao, F. (2016). Electrochemical CO_2 reduction: Electrocatalyst, reaction mechanism, and process engineering. Nano Energy *29*, 439–456. https://doi.org/10.1016/j.nanoen.2016.04.009.

32. Zhang, W., Yang, Y., Li, Y., Li, F., and Luo, M. (2023). Recent progress on integrated CO_2 capture and electrochemical upgrading. Mater. Today Catal *2*, 100006. https://doi.org/10.1016/j.mtcata.2023.100006.

33. Maru, M.S., Ram, S., Shukla, R.S., and Khan, N.u.H. (2018). Ruthenium-hydrotalcite (Ru-HT) as an effective heterogeneous catalyst for the selective hydrogenation of CO_2 to formic acid. Mol. Catal. *446*, 23–30. https://doi.org/10.1016/j.mcat.2017.12.005.

34. Park, J., Valekar, A.H., Oh, K.-R., Awad, A., Song, I.-H., Yoo, C., An, J., and Hwang, Y.K. (2023). Merging biomass and CO_2 utilization; process design and assessment on simultaneous production of lactic acid and formic acid from glycerol and CO_2. Chem. Eng. J. *463*, 142410. https://doi.org/10.1016/j.cej.2023.142410.

35. Moret, S., Dyson, P.J., and Laurenczy, G. (2014). Direct synthesis of formic acid from carbon dioxide by hydrogenation in acidic media. Nat. Commun. *5*, 4017. https://doi.org/10.1038/ncomms5017.

36. Singh, V., Jang, S., Vishwakarma, N.K., and Kim, D.P. (2018). Intensified synthesis and post-synthetic modification of covalent organic frameworks using a continuous flow of microdroplets technique. NPG Asia Mater. *10*, e456. https://doi.org/10.1038/am.2017.209.

37. Yang, Z.Z., Zhang, H., Yu, B., Zhao, Y., Ji, G., and Liu, Z. (2015). A Tröger's base-derived microporous organic polymer: Design and applications in CO_2/H_2 capture and hydrogenation of CO2 to formic acid. Chem. Commun. *51*, 1271–1274. https://doi.org/10.1039/c4cc08295h.

38. Wang, S., Hou, S., Wu, C., Zhao, Y., and Ma, X. (2019). $RuCl_3$ anchored onto post-synthetic modification MIL-101(Cr)-NH_2 as heterogeneous catalyst for hydrogenation of CO_2 to formic acid. Chinese Chem. Lett. *30*, 398–402. https://doi.org/10.1016/j.cclet.2018.06.021.

39. Gunasekar, G.H., Jung, K.-D., and Yoon, S. (2019). Hydrogenation of CO_2 to Formate using a Simple, Recyclable, and Efficient Heterogeneous Catalyst. Inorg. Chem. *58*, 3717–3723. https://doi.org/10.1021/acs.inorgchem.8b03336.

40. Hietala, J., Vuori, A., Johnsson, P., Pollari, I., Reutemann, W., and Kieczka, H. (2016). Formic Acid. In Ullmann's Encyclopedia of Industrial Chemistry (Wiley), pp. 1–22. https://doi.org/10.1002/14356007.a12_013.pub3.

41. Huang, L., Wang, G., Liu, Z., Yan, Z., Zheng, A., and Cao, D. (2022). Single atomic Cu-Anchored 2D covalent organic framework as a nanoreactor for CO_2 capture and in-situ conversion: A computational study. Chem. Eng. Sci. *253*, 117536. https://doi.org/10.1016/j.ces.2022.117536.

42. Broicher, C., Foit, S.R., Rose, M., Hausoul, P.J., and Palkovits, R. (2017). A Bipyridine-Based Conjugated Microporous Polymer for the Ir-Catalyzed Dehydrogenation of Formic Acid. ACS Catal. *7*, 8413–8419. https://doi.org/10.1021/acscatal.7b02425.

43. Cicco, A.D., Aquilanti, G., Minicucci, M., Principi, E., Novello, N., Cognigni, A., and Olivi, L. (2009). Novel XAFS capabilities at ELETTRA synchrotron light source. J. Phys. Conf. Ser. *190*, 12043. https://doi.org/10.1088/1742-6596/190/1/012043.

44. Ravel, B., and Newville, M. (2005). ATHENA , ARTEMIS , HEPHAESTUS : data analysis for X-ray absorption spectroscopy using IFEFFIT. J. Synchrotron Radiat. *12*, 537–541. https://doi.org/10.1107/S0909049505012719.